Comparing the spin period evolution of inactive box-wing satellites and rocket bodies

Nicola Cimmino*[†], Alessandro Vananti* and Thomas Schildknecht*

*Astronomical Institute, University of Bern

Sidlerstrasse 5, 3012, Bern, Switzerland

nicola.cimmino@unibe.ch – alessandro.vananti@unibe.ch – thomas.schildknecht@unibe.ch

[†] Corresponding Author

Abstract

This paper presents a comparative analysis of the long-term spin period evolution of inactive box-wing satellites and rocket bodies. First, it provides an overview of common trends observed at the Astronomical Institute of the University of Bern, across different orbital regimes. In particular, two major behaviours are identified in Medium Earth Orbit: an oscillating pattern and secular trend for box-wing satellites, and a constant trend for rocket bodies. Second, it describes a simulation environment to model such behaviours, adopting an open-source orbital and attitude propagator. The capability to capture these trends is demonstrated, provided an ad-hoc set of initial parameters.

1. Introduction

The growing number of space debris (SD) in Earth's orbit has intensified the demand for effective Active Debris Removal (ADR) strategies to ensure the long-term sustainability of space activities [1]. A key factor in ADR missions is the spin period of the target SD as it directly influences approach and capture strategies.

ADR missions typically require 5 to 10 years from initial design to launch [2], during which the spin characteristics of the target SD can change considerably. This evolution is driven by various environmental torques, including atmospheric drag, solar radiation pressure, Earth's gravitational field, and potential impacts with other objects. Additionally, intrinsic physical properties, such as shape, mass distribution, and surface characteristics (e.g., specular or diffuse reflection), also affect the rate of spin variation. Given these complexities, it is essential not only to determine the current spin period but also to predict its long-term evolution.

Light curves, representing the temporal variation of an object's brightness as observed by optical sensors, are a widely used data source for determining the spin period of space objects [3]. Numerous methods have been proposed in the literature to extract angular velocity (or, equivalently, spin period) from light curves, with the choice of method depending on factors such as observation duration, sampling frequency, data continuity, and whether the data points are evenly spaced in time.

Spectral analysis techniques, such as Fast Fourier Transform, periodogram analysis, and Welch's method [4], are commonly used to estimate a signal's power spectral density (PSD), revealing how the signal's energy is distributed across different frequency components. These methods work by converting the time-domain signal into the frequency domain to identify dominant periodicities. However, a significant limitation of these methods is their reliance on evenly spaced data points.

To address this limitation, alternative techniques have been developed. Epoch folding [5] tests a range of candidate periods by aligning (or "folding") the light curve data to identify periodic behaviour, typically by minimizing the scatter within the folded signal. The Lomb-Scargle periodogram [6] is specifically tailored for unevenly spaced data, providing a robust estimate of the PSD and enabling the detection of significant periodic components. Lately, machine learning techniques have been increasingly applied to estimate spin periods and characteristics of space objects from light curve data, offering advantages in handling large datasets and complex patterns that traditional methods may struggle with [7].

The Astronomical Institute of the University of Bern (AIUB) has extensive experience in the acquisition and analysis of light curve data. Its observational infrastructure is based at the Zimmerwald Observatory, located approximately 10 km south of Bern, Switzerland. Photometric observations have been conducted using the 1-meter Zimmerwald Laser and Astrometry Telescope (ZIMLAT) and the 0.2-meter Zimmerwald Small Aperture Robotic Telescope (ZimSMART) [8]. Using light curves obtained at Zimmerwald, AIUB has successfully determined apparent rotational

periods and their temporal evolution for a wide range of space objects, including box-wing satellites, rocket upper stages, and fragmentation debris, across various orbital regimes [9–11]. Rachman et al. [12] have performed statistical analyses on a set of inactive GLONASS satellites, providing information on the average spin period, average cycle period, and secular trend. They have also developed empirical models to fit observed data and extract future spin periods of GLONASS satellites. Cimmino et al. [13,14] have carried out an extensive sensitivity analysis, examining how different geometries (i.e., panel, parallelepiped, box-wing), initial attitude states, angular velocities, surface properties, and satellite configurations impact the spin behaviour for a space object in Medium Earth Orbit (MEO).

In this context, this paper provides two main contributions. First, it presents an overview of common trends of the spin period of inactive box-wing satellites and rocket bodies observed at AIUB. This includes statistical analyses of relevant parameters such as ranges of values of the spin period across different orbital regimes, and secular trends. Second, a sensitivity analysis by means of simulations is conducted to understand how different parameters influence the spin evolution over time for rocket bodies in MEO, highlighting the main differences with the behaviour of box-wing satellites.

The remainder of this paper is organized as follows. Section 2 presents an overview of AIUB's light curve database, with a particular focus on payloads and rocket bodies, along with relevant statistical insights. Section 3 describes the simulation environment used for the analysis. Section 4 discusses selected simulation results. Finally, Section 5 provides conclusions and outlines directions for future work.

2. AIUB light curve database

The AIUB light curve database currently contains around 4,800 light curves from 544 space objects across different orbital regimes and different types of objects. The database is divided into four orbital regimes, i.e., Low Earth Orbit (LEO), Medium Earth Orbit (MEO), High Eccentric Orbit (HEO) for orbits with an eccentricity larger than 0.2, and Geosynchronous Earth Orbit (GEO), and four object groups.

The first object group is the *payload* (PL) which is usually a box-wing type of object with one or two solar panels attached to the main bus. The second is the *rocket body* (RB) which typically has a cylindrical-like shape. The third is the *debris* which is either mission-related or fragmentation debris. The last one is the *DIS* group for objects discovered during ESA's GEO, GTO, and Molniya surveys. The origin of *DIS*, compared with the other groups, is unknown. As the first two groups represent almost 80% of the whole database, following analyses and considerations will regard only these two groups.

Figure 1 shows the absolute frequency of payloads and rocket bodies across the different orbital regimes. It can be noted that most of the observed objects are rocket bodies, which represent the majority of the observed population in LEO and HEO. Most of MEO objects, instead, are payloads, in particular a set of 70 inactive GLONASS satellites which have been observed from 2015 to 2023.
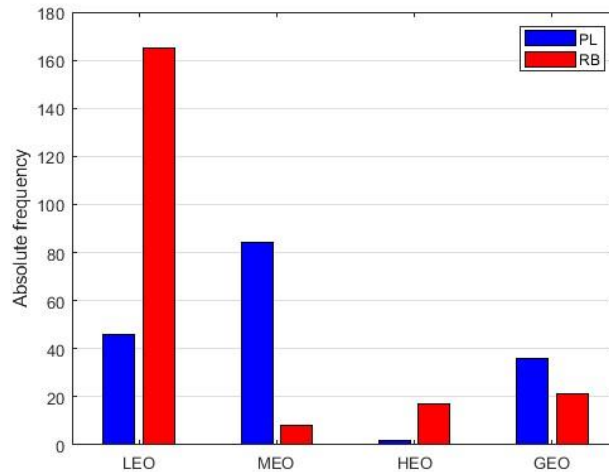

Figure 1: Absolute frequency of payload (PL) and rocket body (RB) objects in AIUB light curve database across the different orbital regimes.

Each light curve in the database undergoes manual processing. Initially, curves with insufficient data (typically fewer than 30 points) are discarded. The remaining cases are divided into two categories: those with no visible repeating

patterns and those that exhibit a periodic behaviour. Non-repeating light curves fall into two subtypes. If the pattern appears flat or overly simple, it likely reflects only the object's orbital motion, indicating no relative rotation during observation; these are termed *stable*. If the pattern is more complex but lacks a clear period, it may suggest a slow rotation with a spin period longer than the observation duration; these are labelled *slow rotators*. For curves showing repetitions, further processing involves cleaning outliers and trends. If the spin period can be successfully extracted, the light curve is classified as *rotator*. If the analysis is inconclusive or remains incomplete due to time constraints, the case is marked as *unfinished*.

To evaluate an object's attitude state over time, the sequence of its light curves is reviewed. Based on this analysis, each object is classified into one of four attitude categories: *Rotator*, *Slow Rotator*, *Stable*, or *Unknown*.

An object is labelled a *Rotator* if it has at least one processed light curve indicating rotation, regardless of whether it also shows slow or stable behaviour at other times. If no rotator light curve is found, the object is classified based on the relative frequency of slow rotator and stable light curves; *Slow Rotator* status takes precedence if both counts are equal. An object is considered *Stable* only if stable light curves significantly outnumber slow rotators. The *Unknown* category includes objects for which attitude determination is not possible due to poor data quality, incomplete processing, or a lack of processed light curves.

Figure 2 shows the absolute frequency of payload and rocket bodies with respect to the attitude state. Rotators (39.2%) and stable (32.1%) objects make up the largest groups. While the former are distributed across all orbital regimes, the latter were not observed in HEO. Payloads dominate the *Rotator* group (70.1%), whereas rocket bodies are the majority in both the *Slow Rotator* (65.2%) and *Stable* (81.8%) categories. The prevalence of slow rotator and stable LEO rocket bodies suggests a trend of rotational decay in LEO rocket bodies, likely driven by eddy current torque [15]. Another key finding is the high count of rotator and stable rotator MEO payloads, most of which are GLONASS satellites (83.7%).
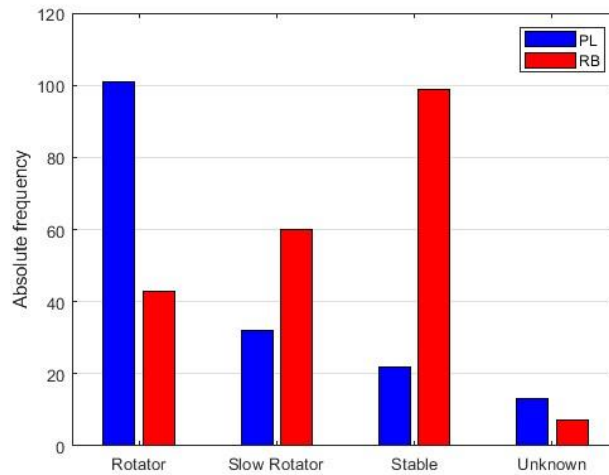

Figure 2: Absolute frequency of payload (PL) and rocket body (RB) objects in AIUB light curve database across different attitude states.

A visual analysis of spin period evolution for *Rotator* objects revealed three main behaviour patterns: *Oscillating*, *Increasing*, and *Decreasing*. Based on this, rotators were grouped accordingly, with an additional *No Trend* category for cases lacking enough data or successful period extractions. The database includes 72 objects with unknown trends, 42 oscillating rotators, 12 increasing and 18 decreasing behaviour patterns.

Figure 3 shows the absolute frequency of payload and rocket bodies with respect to the spin period pattern. Oscillating rotators are mostly MEO payloads, specifically GLONASS satellites, with only one exception, a BREEZE-M rocket body in GEO. Increasing and decreasing rotators are more varied in orbit and object type.
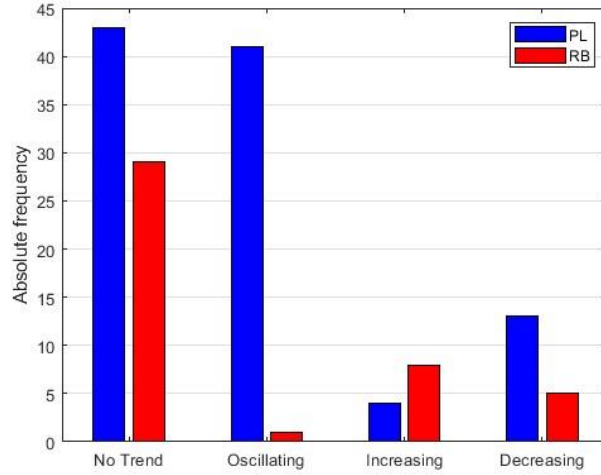
Figure 3: Absolute frequency of payload (PL) and rocket body (RB) objects in AIUB light curve database across different rotating patterns.

The spin periods of objects in the database range from less than 1 s to nearly 1 500 s (25 min.). The fastest spinner is a GEO rocket body, BREEZE-M R/B (COSPAR ID: 2015-075B), with a period of 0.88 s (410.26 °/s), while the slowest is a GEO payload, COSMOS 2473 (COSPAR ID: 2011-048A), with a period of 1 480.51 s (0.24 °/s). Figure 4 shows the minimum (lower whisk), maximum (upper whisk) and median value (dot marker) of the logarithm base 10 of the apparent spin period (P_a) across the different orbital regimes, for payload (blue markers) and rocket body (red markers) objects. Rocket bodies tend to be fast rotators across all orbital regions, with median spin periods smaller than 7 s in all regions except HEO, where they still spin fastest among object types (median of circa 43 s). Payloads show more diverse spin behaviours. LEO payloads are relatively fast (median of circa 11.6 s); slower payloads are mainly found in MEO and GEO. The highest payload median (820 s in HEO) is skewed by a single object: MAQSAT H (COSPAR ID: 1997-066 A).
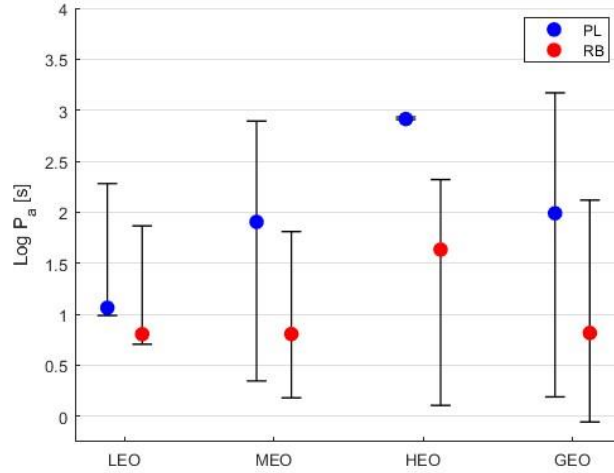

Figure 4: Minimum, maximum and median apparent spin period of payload (PL) and rocket body (RB) objects across different orbital regimes.

From 2015 to 2023, AIUB was in particular observing 70 decommissioned satellites of the Russian Global Navigation Satellite System, GLONASS. Observed data of some of the GLONASS satellites show a periodic variability of the spin period and a secular (increasing/decreasing) trend. Figure 5 shows the spin period time evolution for GLONASS satellites Cosmos 1988 (NORAD 19750) (a) and Cosmos 2204 (NORAD 22057) (b), both exhibiting an oscillating pattern with a secular decreasing/increasing trend. In the same period, different rocket bodies were also observed at the same orbital regime, namely Ariane 5 [16], Atlas V Centaur [17], Fregat [18] and SL-12 [19]. Observed data of

these RBs show instead a constant value of the apparent spin period. Figure 6 shows the spin period time evolution for Ariane 5 (NORAD 41863) (a) and SL-12 (NORAD 33383) (b), both exhibiting a constant P_a over a period of 8 and 10 years respectively.
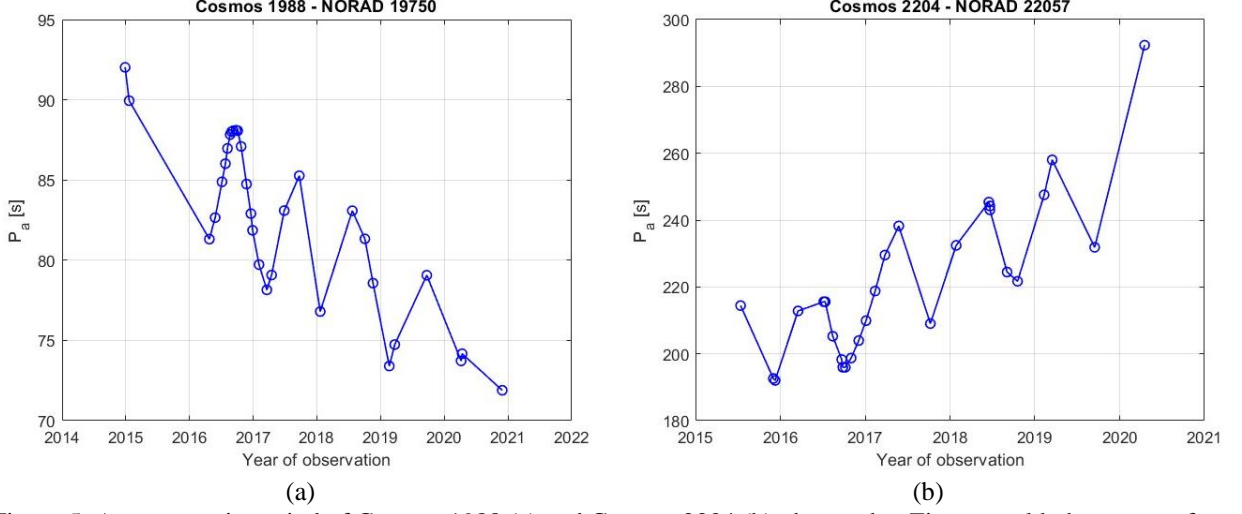

Figure 5: Apparent spin period of Cosmos 1988 (a) and Cosmos 2204 (b) observed at Zimmerwald observatory from 2015 to 2021.
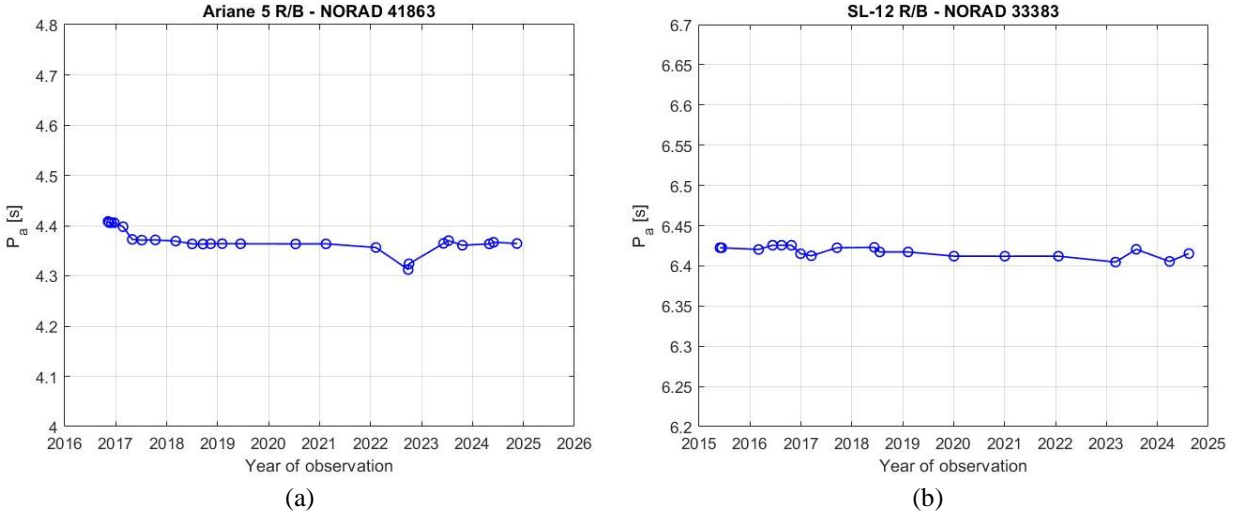

Figure 6: Apparent spin period of Ariane 5 R/B (a) and SL-12 R/B (b) observed at Zimmerwald observatory from 2015 to 2025.

3. Simulation environment

To model the long-term pattern of the spin period, an opensource software, namely Debris Spin/Orbit Simulation Environment (D-SPOSE) [20], has been adopted, which integrates three coupled differential equations. First, the dynamics equation for orbital motion in Earth-Centred Inertial frame:

$$\ddot{\boldsymbol{r}}(t) = -\frac{\mu}{r(t)^3}\boldsymbol{r}(t) + \sum_j \boldsymbol{a}_j(t, \boldsymbol{r}(t), \boldsymbol{v}(t), \boldsymbol{q}(t), \boldsymbol{\omega}(t)) \tag{1}$$

where $\boldsymbol{r}$ is the position as a function of time t, $r = \|\boldsymbol{r}\|$, $\boldsymbol{v}$ is the velocity, $\boldsymbol{q}$ is the attitude parametrization, chosen here to be a quaternion, $\boldsymbol{q} = [q_0 \ \boldsymbol{q}_v^T]^T$, $\boldsymbol{\omega}$ is the angular velocity of the body with respect to the inertial frame, μ is the

Earth's gravitational parameter, and $\boldsymbol{a}_j$ represents the additional considered accelerations due to orbital perturbations, which are a function of the rigid body's position, velocity, and attitude state.
Second, the attitude dynamics equation:

$$\boldsymbol{I\dot{\omega}}(t) + \boldsymbol{\omega}(t)^{\times}\boldsymbol{I\omega}(t) = \sum_{j} \boldsymbol{\tau}_j(t, \boldsymbol{r}(t), \boldsymbol{v}(t), \boldsymbol{q}(t), \boldsymbol{\omega}(t)) \tag{2}$$

where $\boldsymbol{\tau}_j$ represents the external torques, $\boldsymbol{I}$ is the matrix representation of the inertia tensor of the rigid body in the centroidal body-fixed frame. The superscript $\times$ denotes the skew-symmetric matrix representation of the cross-product. Finally, the kinematic equation for the absolute orientation of the spacecraft:

$$\dot{\boldsymbol{q}}(t) = \frac{1}{2}\boldsymbol{\Omega}(\boldsymbol{\omega})\boldsymbol{q}(t) \tag{3}$$

where, being ω_x, ω_y and ω_z the angular velocity components in the body-frame, $\boldsymbol{\Omega}$ is defined as follows.

$$\boldsymbol{\Omega} = \begin{bmatrix} 0 & -\omega_x & -\omega_y & -\omega_z \\ \omega_x & 0 & \omega_z & -\omega_y \\ \omega_y & -\omega_z & 0 & \omega_x \\ \omega_z & \omega_y & -\omega_x & 0 \end{bmatrix} \tag{4}$$

Equations (1)-(3) are numerically propagated at a fixed integration time step using the Runge-Kutta Dormand-Prince (RKDP) numerical integration method [21]. The same time step is used for propagating both the orbit and attitude equations as both are coupled.
The spin period (T) is then computed using the following equation.

$$T(t) = \frac{2\pi}{|\boldsymbol{\omega}(t)|} \tag{5}$$

Four input files are required to run the simulator:
- a Two-Line Elements (TLE) file corresponding to the initial epoch to extract the initial orbital elements.
- a file containing the propagation parameters, among which the propagation time step and the propagation time.
- a file containing the model parameters (i.e., external perturbations). For the MEO regime, the following perturbations have been considered: asymmetry of the gravitational field (only J2), third-body (Sun and Moon), Solar Radiation Pressure (SRP), gravity gradient torque, and SRP torque. Moreover, the initial attitude of the SD is described as a rotation of the Body Reference Frame (BRF) with respect to the Orbital Reference Frame (ORF) [22] with a classical (3-2-1)-sequence of Euler angles: yaw (ψ), pitch (θ) and roll (ϕ). Similarly, the initial angular velocity is expressed in terms of components of $\boldsymbol{\omega}$ in the BRF.
- a file containing information on the SD geometry. Any SD shape can easily be considered since the input consists of a list of triangular surfaces defined by the position of its three vertices in the BRF, the direction of its inward surface normal and the optical coefficients in the visible spectra. In particular, the surface properties are described by the coefficient of specular reflection (ρ), diffusive reflection (δ) and absorption (α). The three coefficients must satisfy the following constraint.

$$\rho + \delta + \alpha = 1 \tag{6}$$

4. Results and discussions

To compare the long-term time evolution of the spin period of box-wing inactive satellites and rocket bodies, a sensitivity analysis has been carried out. The initial orbital state is assumed to be fixed. In particular, the initial orbital elements, namely, semimajor axis (a), eccentricity (e), inclination (i), right ascension of the ascending node (Ω), argument of perigee (ω) and true anomaly (ν), are extracted from the TLE [23] of COSMOS 2109 (NORAD ID 21006) at epoch 29th June 2015, 16:29:34 UTC (see Table 1). The propagation time is 1825 days, the integration step is 1 s, and the sampling frequency of the output is 1 state/12 h. Two geometries are considered: a box-wing configuration and

a rocket-body model, which are described in detail in the following subsections. For both geometries, the BRF-axes coincide with the central axes of inertia of the SD. Moreover, the BRF is initially aligned with the ORF. For each geometry, the following settings have been explored (see Table 2):

- 4 initial attitudes: one assumes that there is no rotation of the BRF with respect to the ORF, and three assume a 90 ° rotation of yaw, pitch and roll respectively.
- 5 initial angular velocities: one assumes that the initial angular velocity is zero. This is representative of a very low speed case. Then, three assume an angular velocity of 5 °/s along each axis of inertia respectively. Finally, it is assumed an angular velocity component of 3.0 °/s along all the three axes of inertia, resulting in $|\boldsymbol{\omega}(t)|$ equal to 5.2 °/s.
- 3 surface properties distributions, namely, all surfaces have either specular reflection, diffusive reflection or absorption properties. Additional asymmetric distributions have been considered for the different geometries as it will be detailed later in the subsections.

Table 1: Initial orbital elements for the simulation.

a [km]	e [-]	i [°]	Ω [°]	ω [°]	ν [°]
25509.4	0.0082	64.1	208.8	186.2	339.0

Table 2: Model parameters for the sensitivity analysis.

Parameters	Values
$[\psi\ \theta\ \phi]$ °	$[0\ 0\ 0], [90\ 0\ 0], [0\ 90\ 0], [0\ 0\ 90]$
$[\omega_x\ \omega_y\ \omega_z]$ °/s	$[0\ 0\ 0], [5\ 0\ 0], [0\ 5\ 0], [0\ 0\ 5], [3\ 3\ 3]$
$[\rho\ \delta\ \alpha]$	$[1\ 0\ 0], [0\ 1\ 0], [0\ 0\ 1]$

4.1 Results for the box-wing model

In a previous study [13], the authors have carried out a wide sensitivity analysis of the spin period time evolution for a generic box-wing satellite, located on a MEO orbit, varying the optical coefficients, the initial angular velocity, and the initial attitude state assuming the values reported in Table 2. Moreover, the variation of the canting angle of the solar panels with respect to the central bus has also been explored. Two configurations have been considered: a symmetric one in which both panels are rotated of the same angle β, and an asymmetric case in which the left and right solar panels are rotated of β and $-\beta$ respectively. In the former case, β can assume a value of $\{0, 45, 90, 135\}$ °; in the latter case β can assume a value of $\{5, 10, 15\}$ °. The outcomes of [13] constraint the initial conditions for the analyses in this work. In particular, to have an oscillating pattern and a secular trend of the spin period, two conditions are necessary: an asymmetric configuration of the canting angles, and an asymmetry in the surface properties.

In this work, a GLONASS I satellite has been used as reference for the simulations. The spacecraft has been modelled as a box-wing satellite with the following characteristics: a central box of size $4.0 \times 2.0 \times 2.0$ m, and two solar panels of size $0.0 \times 3.5 \times 4.0$ m canted with β equal to 5 ° (see Figure 7). The total mass of the satellite is 1400 kg [24] and the inertia matrix is:

$$\boldsymbol{I} = \begin{bmatrix} 1709.5 & 0 & 0 \\ 0 & 2305.3 & 0 \\ 0 & 0 & 2915.2 \end{bmatrix} kg\ m^2 \tag{7}$$

Fixed the geometry and the mass distribution, two test cases are described. The model parameters for the first box-wing test case (BW1) are the following:

- Surface properties. Central box, +X face: $\rho = 1.0$; central box, -X, $\pm$ Y and $\pm$ Z faces: $\delta = 1.0$; solar panels, +X face: $\rho = 0.25, \delta = 0.25, \alpha = 0.50$; solar panels, -X face: $\delta = 1.0$.
- Initial attitude: $[\psi, \theta, \phi] = [0, 0, 90]$ °.
- Initial angular velocity: $[\omega_x, \omega_y, \omega_z] = [0, 6.6, 0]$ °/s.

Figure 8 (a) shows the time evolution of the spin period using the parameters above. Two important features have been captured by the model and can be clearly noted in the figure: a yearly periodicity of T due to the yearly cycle of the Sun apparent motion around the Earth, and a decreasing secular trend (i.e., the spacecraft is spinning up). The former feature is attributable to the asymmetric canting angle, whereas the latter is due to the asymmetry of the surface properties.

For the second box-wing test case (BW2), the same canting angle and initial attitude as BW1 are set, but different setting for:

- Surface properties. Central box, +X face: $\rho = 1.0$; central box, -X, ± Y and ± Z faces: $\alpha = 1.0$; solar panels, +X face: $\rho = 0.25$, $\delta = 0.25$, $\alpha = 0.50$; solar panels, -X face: $\delta = 1.0$.
- Initial angular velocity: $[\omega_x, \omega_y, \omega_z] = [3.8, 3.8, 3.8]$ °/s.

In this case (Figure 8 (b)) the spin period exhibits a yearly periodicity, as seen before, but an increasing secular trend (i.e., the spacecraft is slowing down). Also in this case, the two features can be attributable to the asymmetry of the canting angle and the asymmetry of the surface properties, respectively.

A few differences can be noticed when comparing observed and simulated data. The amplitude of the oscillations and the slope of the secular trend are larger in the simulated scenario. Moreover, observed data exhibit sharper variations of the spin period, with a characteristic "triangular" pattern. Such discrepancies can be attributable to the initial set of modelling parameters as well as to mismatches in the geometric and mass distribution properties of the modelled spacecraft.
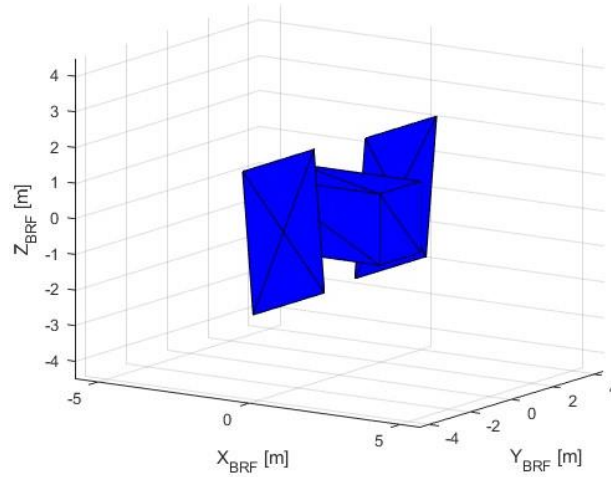

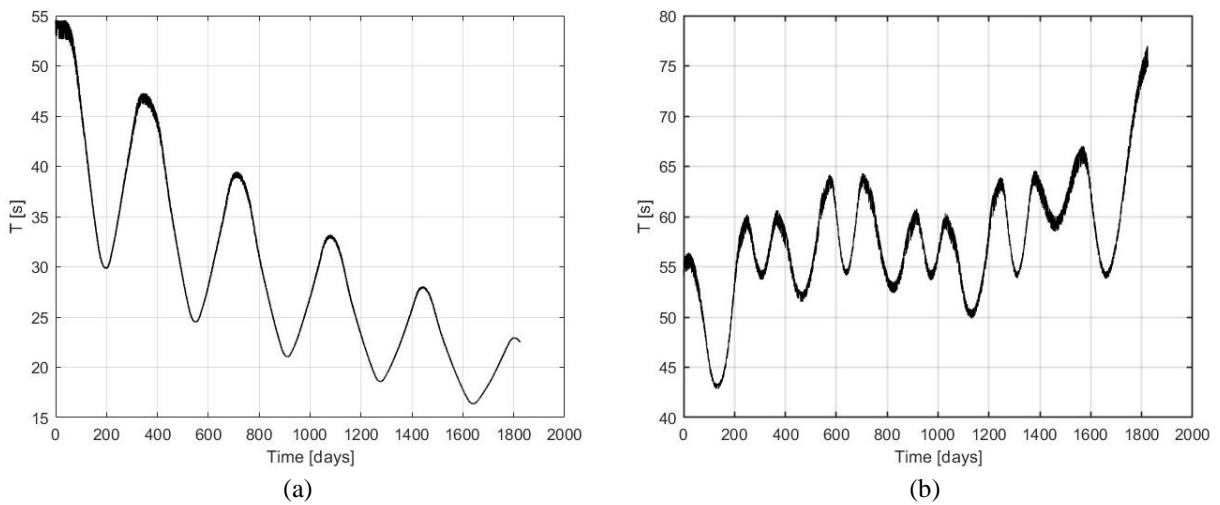Figure 7: Meshed model of a GLONASS I satellite.

(a)   (b)

Figure 8: Modelled spin period for BW1 (a) and BW2 (b).

4.1 Results for the rocket-body model

In this work, an Atlas V Centaur R/B [17] has been used as reference for the simulations. The RB has been modelled as an octagonal prism with the following characteristics: the bases are octagons inscribed in a circle of radius 1.5 m, and the height is 9 m (see Figure 9 (a)). The total mass of the satellite is 2300 kg [20] and the inertia matrix is:

$$I = \begin{bmatrix} 16717.3 & 0 & 0 \\ 0 & 16717.3 & 0 \\ 0 & 0 & 2384.6 \end{bmatrix} kg\ m^2 \tag{8}$$

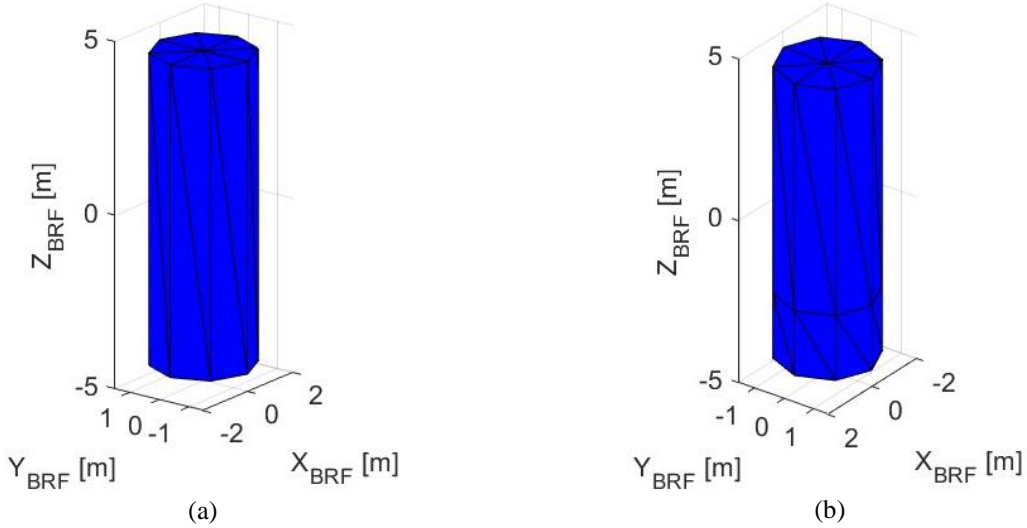(a)   (b)

Figure 9: Meshed model of the rocket body for symmetric (a) and asymmetric (b) surface properties modelling.

First, results for symmetric surface properties are presented. Regardless of the specific surface properties (i.e., specular reflection, diffusive reflection or absorption), the spin period remains bounded around a mean value. Nevertheless, depending on the initial attitude state, the behaviour of the angular velocity components changes over time. In particular:

- if the initial angular velocity is 0 °/s, ω_x (or ω_y) will oscillate around a mean non-zero value, ω_y (or ω_x) will oscillate around zero and ω_z will be equal to zero for the whole propagation time (see Figure 10 (a));
- if the initial angular velocity is along one of the inertia axes, it will remain along the same axis for the whole propagation time, whereas the remaining two components will be equal to zero (see Figure 10 (b));
- if the initial angular velocity has equal components along all the axes, then the ω_z component will keep the same value for the whole propagation time, whereas ω_x and ω_y will oscillate around zero, shifted of circa 1 day with respect to each other (see Figure 10 (c) and the zoomed in Figure 10 (d)).
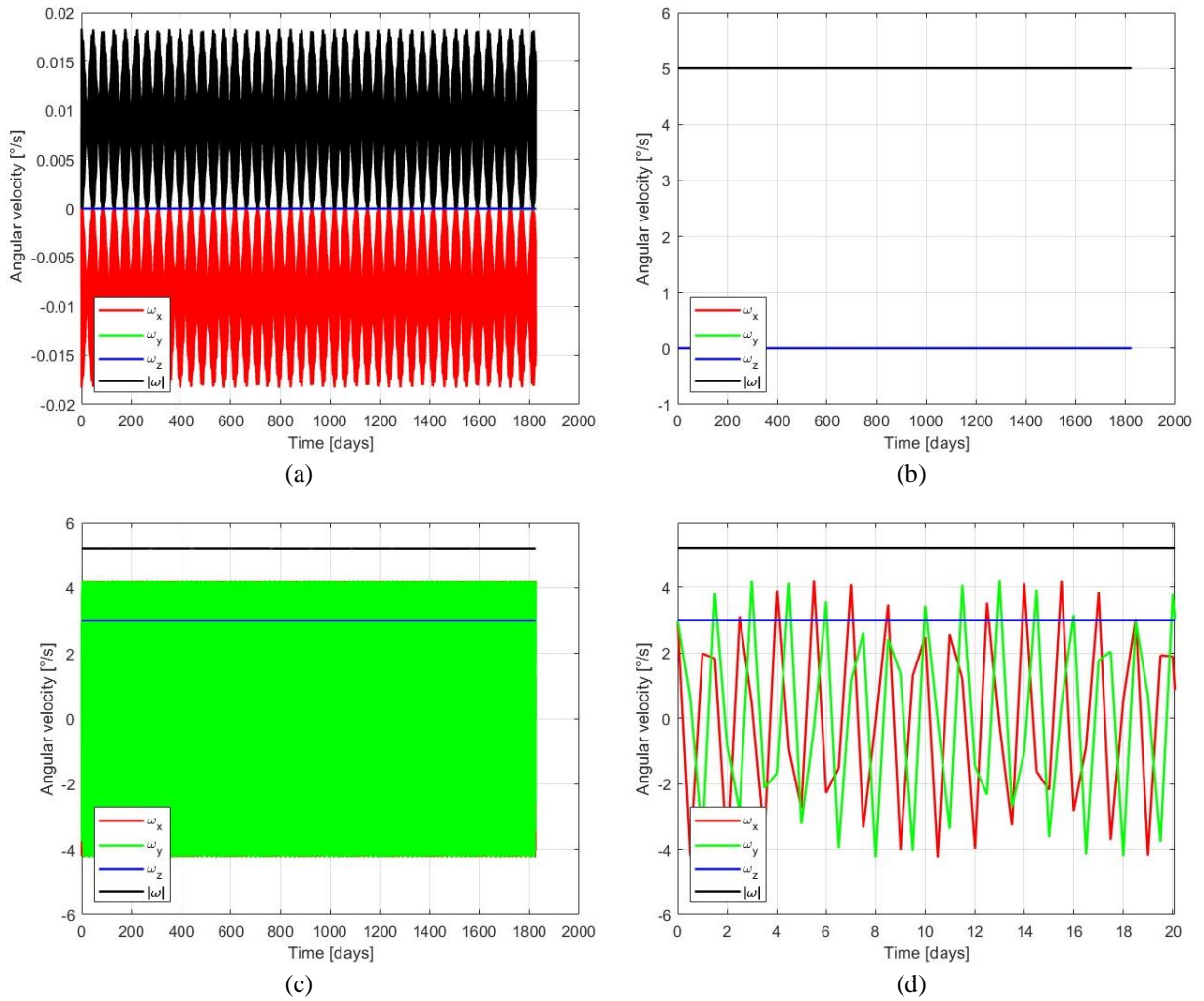
9

Figure 10: Angular velocity components for symmetric surface properties. The initial angular velocity is 0 °/s (a), or is along a central axis of inertia (b), or has components along all the axes of inertia (c-d).

In the next analysis, asymmetries in the surface properties are introduced. Two major asymmetries are considered:
- the bases have all diffusive properties, $[\rho\ \delta\ \alpha]$ = [0 1 0]. Half of the side surface has diffusive properties, $[\rho\ \delta\ \alpha]$ = [0 1 0], and half has absorption properties, $[\rho\ \delta\ \alpha]$ = [0 0 1].
- the original prism is split in two prisms of height 7 m and 2 m respectively (see Figure 9 (b)). The upper base and the first cylinder side surface have diffusive properties, $[\rho\ \delta\ \alpha]$ = [0 1 0]. The lower base and the second cylinder side surface have specular properties, $[\rho\ \delta\ \alpha]$ = [1 0 0].

In both cases, regardless of the initial attitude state, the spin period remains equal to its initial value or bounded around a mean value (for the low-speed case). Moreover, if the initial angular velocity is along the minimum axis of inertia or has components along all the axes, the same behaviour of the corresponding symmetric surface properties-case is observed. If the initial angular velocity is along an axis of maximum inertia, ω_z remains zero for the whole propagation time, whereas ω_x (or ω_y) oscillates around a mean value slightly different to 5 °/s and ω_y (or ω_x) oscillates around a mean value slightly different to 0.0 °/s, as it can be seen in Figure 11 (a) (or Figure 11 (b)). The spin period remains constant and slightly larger (or smaller) than 72 s.

It is important to note that in the case of symmetric surface properties, the SRP torque is 0.0 N·m due to the symmetry of both the geometry and the surface characteristics. In contrast, when surface properties are asymmetric, the total SRP torque acting on the rocket body is on the order of 10^{-5} N·m, comparable to the torque experienced by the box-wing configuration. However, in the rocket body case, this torque does not induce a secular trend, probably owing to its higher moments of inertia and the different behaviour of the torque components. This aspect will be examined in more detail in future work.
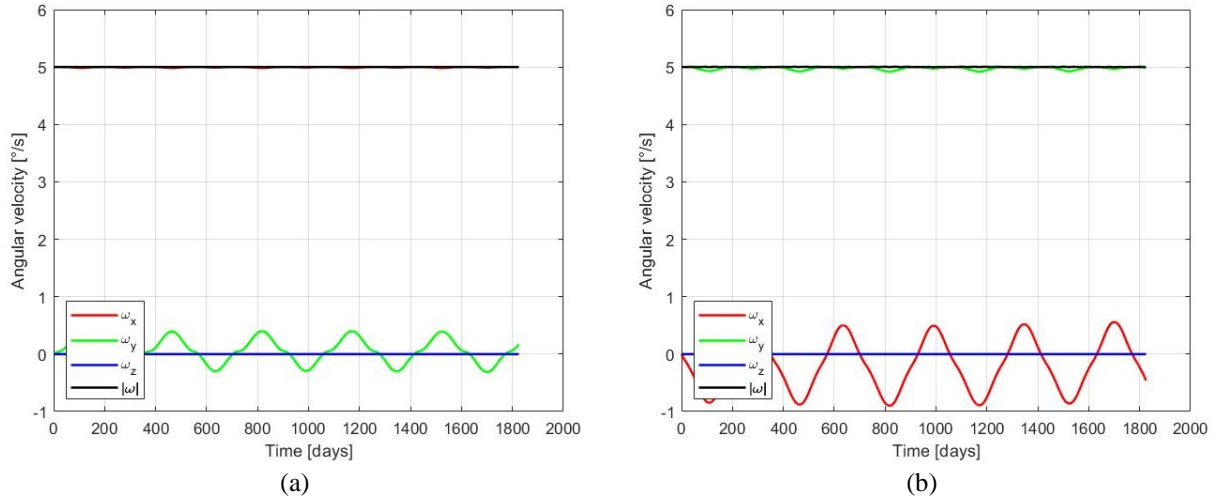
Figure 11: Angular velocity components for asymmetric surface properties. The initial angular velocity is along an axis of maximum inertia, i.e., X_{BRF} (a) or Y_{BRF} (b).

5. Conclusions

This paper has presented a comparative analysis of the long-term spin period evolution of inactive box-wing satellites and rocket bodies. First, an overview of the AIUB database is provided, showing that rocket bodies constitute the majority of observed objects in LEO and HEO, while MEO is dominated by payloads. *Rotators*, (i.e., objects for which the spin period can be successfully extracted), and *Stable* objects (i.e., objects with no clear patterns in the light curve) form the largest categories; rotators are distributed across all orbital regimes, whereas stable objects are absent in HEO. Payloads dominate the rotator group (70.1%), while rocket bodies are most common among *Slow Rotators* (65.2%) and stable objects (81.8%).

Spin period trends indicate that *Oscillating* rotators are mostly MEO payloads (mainly GLONASS), except for a single BREEZE-M rocket body in GEO. In contrast, increasing and decreasing rotators span multiple orbits and object types. Rocket bodies generally exhibit fast rotation across all orbits, with median spin periods under 7 seconds, except in HEO (~43 s), where they still spin faster than other objects. Payloads show more varied spin behaviours.

Due to the large number of GLONASS satellites observations, further analysis focused on MEO region. In particular, while the spin period of inactive GLONASS satellites display oscillating patterns with secular trends, rocket bodies maintain nearly constant spin periods over observation spans up to 10 years.

To understand and model these trends, a simulation environment using the open-source D-SPOSE tool was employed. Two meshed models, one for a box-wing satellite and one for a rocket body, were generated. For box-wing objects, initial conditions have been constrained based on prior authors' works, introducing asymmetries in canting angles and surface properties. With appropriate initial conditions, the model successfully reproduced the 1-year periodic oscillations and secular trends.

For the rocket bodies, a broad range of initial attitudes, angular velocities and surface properties (symmetric and asymmetric) has been explored. Across all cases, the spin period remains constant, or bounded around a mean value, for the whole propagation time, aligning with observational data. Notably, even in cases where the angular velocity components exhibit periodic variations, the overall rotational speed remains constant.

Further analyses should be carried out to reduce discrepancies between modelled and observed data. This includes further tuning of the initial attitude state and optical coefficients, as well as a higher fidelity model of the box-wing geometry. Moreover, the long-term evolution of the spin period in other orbital regimes will also be investigated.

References

[1]   ESA Space Debris Office. 2024. ESA's Annual Space Environment Report. Darmstadt, Germany.
[2]   White, A.E. and Lewis, H.G. 2014. An adaptive strategy for active debris removal. *Advances in Space Research*, 53. https://doi.org/10.1016/j.asr.2014.01.021

[3]   Šilha, J., Pittet, J.N., Hamara, M. and Schildknecht, T. 2018. Apparent rotation properties of space debris extracted from photometric measurements. *Advances in Space Research*, 61. https://doi.org/10.1016/j.asr.2017.10.048

[4]   Linder, E., Silha, J., Schildknecht, T. and Hager, M. 2015. Extraction of spin periods of space debris from optical light curves. *Proceedings of the International Astronautical Congress, IAC*.

[5]   Larsson, S. 1996. Parameter estimation in epoch folding analysis. *Astronomy and Astrophysics Supplement Series*, 117. https://doi.org/10.1051/aas:1996150

[6]   Isoletta, G., Opromolla, R. and Fasano, G. 2025. Attitude motion classification of resident space objects using light curve spectral analysis. *Advances in Space Research*, 75, 1077–95. https://doi.org/10.1016/j.asr.2024.10.034

[7]   Badura, G.P., Christopher, · and Valenta, R. 2024. Physics-Guided Machine Learning for Satellite Spin Property Estimation from Light Curves. *The Journal of the Astronautical Sciences 2024 71:5*, Springer. 71, 1–36. https://doi.org/10.1007/S40295-024-00464-5

[8]   Herzog, J., Schildknecht, T., Hinze, A., Ploner, M. and Vananti, A. 2013. Space Surveillance Observations at the AIUB Zimmerwald Observatory. *Sixth European Conference on Space Debris, Darmstadt, Germany*.

[9]   Vananti, A., Lu, Y. and Schildknecht, T. 2023. Attitude Estimation of H2A Rocket Body from Light Curve Measurements. *International Journal of Astrophysics and Space Science*. https://doi.org/10.11648/j.ijass.20231102.11

[10]   Rachman, A., Schildknecht, T. and Vananti, A. 2018. Analysis of temporal evolution of debris objects' rotation rates inside AIUB light curve database. *Proceedings of the International Astronautical Congress, IAC*.

[11]   Vananti, A., Guthruf, D., Lu, Y. and Schildknecht, T. 2021. Estimation of Reflective Properties from Light Curves of a H2a Rocket Body. *8th European Conference on Space Debris*.

[12]   Rachman, A., Vananti, A. and Schildknecht, T. 2025. Spin Period Evolution of Decommissioned GLONASS Satellites. *Aerospace 2025, Vol 12, Page 283*, Multidisciplinary Digital Publishing Institute. 12, 283. https://doi.org/10.3390/AEROSPACE12040283

[13]   Cimmino, N., Vananti, A. and Schildknecht, T. 2025. Predicting the Time Evolution of Space Debris Spin Period for Active Debris Removal Missions. *9th European Conference on Space Debris,* Bonn, Germany.

[14]   Cimmino, N., Vananti, A. and Schildknecht, T. 2025. Modelling the Oscillating Pattern of the Apparent Spin Period of Inactive GLONASS Satellites. *IEEE 12th International Workshop on Metrology for AeroSpace*, Naples, Italy.

[15]   Lin, H.Y., Zhu, T.L., Liang, Z.P., Zhao, C.Y., Wei, D., Zhang, W. et al. 2019. Tiangong-1's accelerated self-spin before reentry. *Earth, Planets and Space*, 71. https://doi.org/10.1186/s40623-019-0996-8

[16]   Pinardell Pons, A. and Noomen, R. 2019. Ariane 5 GTO debris mitigation using natural perturbations. *Advances in Space Research*, Elsevier Ltd. 63, 1992–2002. https://doi.org/10.1016/j.asr.2018.12.001

[17]   Ravi, P., Black, A. and Frueh, C. 2023. Investigation of Atlas V Centaur Upper Stage Fragmentation Events. *Journal of the Astronautical Sciences*, 70. https://doi.org/10.1007/s40295-023-00377-9

[18]   Zarcone, G., Rossetti, M., Hadji Hossein, S. and Piergentili, F. 2022. A graphical method for the analysis of a satellite's in-orbit breakup through optical observations. *Advances in Space Research*, 70. https://doi.org/10.1016/j.asr.2022.05.032

[19]   Pearce, E.C., Weiner, B. and Krantz, H. 2020. Examining the effects of on-orbit aging of SL-12 rocket bodies using visible band spectra with the MMT telescope. *Journal of Space Safety Engineering*, **7**. https://doi.org/10.1016/j.jsse.2020.07.017

[20]   Sagnières, L.B.M., Sharf, I. and Deleflie, F. 2020. Simulation of long-term rotational dynamics of large space debris: A TOPEX/Poseidon case study. *Advances in Space Research*, 65. https://doi.org/10.1016/j.asr.2019.11.021

[21]   Dormand, J.R. and Prince, P.J. 1980. A family of embedded Runge-Kutta formulae. *Journal of Computational and Applied Mathematics*, 6. https://doi.org/10.1016/0771-050X(80)90013-3

[22]   Vallado, D. and McClain, W. 2007. Fundamentals of astrodynamics and applications. *Space Technology Library, Microcosm Press & Kluwer Academic Publishers*.

[23]   Space-Track.Org. Last access: 15.06.2025.

[24]   Revnivykh, S., Bolkunov, A., Serdyukov, A. and Montenbruck, O. 2017. GLONASS. *Springer Handbooks*, Springer. 219–45. https://doi.org/10.1007/978-3-319-42928-1_8